





Article

Local Crystalline Structure of Doped Semiconductor Oxides Characterized by Perturbed Angular Correlations: Experimental and Theoretical Insights

Anastasia Burimova *, Artur Wilson Carbonari *, Nicole Pereira de Lima, Arnaldo Alves Miranda Filho, Alexandre Pinho dos Santos Souza, Tatiane da Silva Nascimento Sales, Wanderson Lobato Ferreira, Luciano Fabricio Dias Pereira, Bruno Santos Correa  and Rajendra Narain Saxena 

Instituto de Pesquisas Energéticas e Nucleares IPEN-CNEN/SP, São Paulo 05508-000, Brazil

* Correspondence: anstburimova@gmail.com (A.B.); carbonar@ipen.br (A.W.C.)

Abstract: Doping semiconductor oxides with trace amounts of non-native elements can improve their properties such as bandgap and conductivity. The lack of local techniques makes the precise characterization of these materials difficult. Among the few techniques capable of providing local characterization, those based on hyperfine interactions at probe nuclei have the advantage of being well established, probing the material homogeneously and completely, thus investigating different regions of material. Some of these techniques are also quite sensitive even at extremely low dopant concentrations. The perturbed angular correlation technique, combined with first-principles calculations, has recently been shown to be a powerful method for characterizing doped semiconductor oxides. In this paper, we present a brief review of the unique information extracted from the semiconductor investigation with such a complex approach, including semiconductor oxides doped with cadmium and other elements. A strong relationship between the local environment, including electronic structure, and the nature of the dopant and the native element of the doped oxides is also shown.

Keywords: doping; semiconductor oxides; hyperfine interactions; perturbed angular correlations



Citation: Burimova, A.; Carbonari, A.W.; de Lima, N.P.; Miranda Filho, A.A.; dos Santos Souza, A.P.; da Silva Nascimento Sales, T.; Ferreira, W.L.; Pereira, L.F.D.; Correa, B.S.; Saxena, R.N. Local Crystalline Structure of Doped Semiconductor Oxides Characterized by Perturbed Angular Correlations: Experimental and Theoretical Insights. *Crystals* **2022**, *12*, 1204. <https://doi.org/10.3390/cryst12091204>

Academic Editor: Francisco M. Morales

Received: 17 July 2022

Accepted: 11 August 2022

Published: 26 August 2022

Publisher's Note: MDPI stays neutral with regard to jurisdictional claims in published maps and institutional affiliations.



Copyright: © 2022 by the authors. Licensee MDPI, Basel, Switzerland. This article is an open access article distributed under the terms and conditions of the Creative Commons Attribution (CC BY) license (<https://creativecommons.org/licenses/by/4.0/>).

1. Introduction

Doping is an extremely popular method of tailoring the properties of the materials, aimed at improving their performance in diverse applications. The control over macroscopic properties is essential in a search for most appropriate doping conditions, such as solute specification and concentration. Doping-induced perturbation of macroscopic properties may originate directly or indirectly (collective phenomena) from local effects. Hence, it makes sense to employ some exclusive tools suitable for high-quality characterization of doped materials at the subnanoscopic level.

Time-differential perturbed angular correlation spectroscopy (TDPAC spectroscopy, or shortly TDPAC), an unconventional hyperfine-interaction-based characterization method, demonstrates an exceptionally high capacity as a technique for probing local electronic structure. The time window of TDPAC permits taking account of both static and dynamic effects (if present) revealing the peculiarities of charge distribution at the atomic sites as well as the fluctuations of this distribution. This is achieved by incorporation of the probe atoms into the host system, where they are expected to substitute indigenous atoms. Thus, inclusion of TDPAC probes is equivalent to a high dilution doping. The commonly employed γ - γ TDPAC-suited isotopes are ^{111}Cd , originating either from the decay of ^{111}In or ^{111m}Cd , and ^{181}Ta , originating from ^{181}Hf . TDPAC yields information on the electric field gradient (EFG), commonly represented by a rank 2 tensor \mathcal{V}_{ij} , or briefly by its major component V_{zz} and asymmetry parameter $\eta = (|V_{yy}| - |V_{xx}|)/|V_{zz}|$, being $\{V_{xx}, V_{yy}, V_{zz}\}$ the \mathcal{V}_{ij} eigenset, $|V_{xx}| \leq |V_{yy}| \leq |V_{zz}|$.

Previously, TDPAC was employed for general research on the structure of crystalline systems, for instance, for the rectification of the data obtained by conventional methods (see, e.g., [1]). In this line, the technique already required a complementary theoretical structure modeling for data interpretation, and a simple point charge model (PCM) was adopted. It was further superseded by *ab initio* density-functional-theory-based simulations (shortly, DFT) that allowed a far more effective extraction of information of incomparably higher reliability. The TDPAC+DFT combo, to be discussed in the present review, allows insights on the dopant-induced structure modulations, charge relocalization, and trapping effects among other phenomena.

For this review, a series comprising ZnO, SnO, Sc₂O₃, Y₂O₃, In₂O₃, TiO₂, SnO₂, and CeO₂, i.e., (II), (III), and (IV)-valent oxides, with available TDPAC and appropriate DFT studies was selected [2–12], so that TDPAC probes Cd and Ta could represent iso- and heterovalent dopants. Moreover, in (III)- and (IV)-valent oxides Cd²⁺ and Ta⁵⁺ ions become acceptor and donor impurities. Thus, with respect to the relative charge of the host and guest ions, the aforementioned set is exhaustive. For the selected trivalent oxides, the ionic radii of Sc, In, and Y in sixfold coordination lie between those of Ta and Cd, allowing to track structure relaxations when the size of the dopant ion is either smaller or greater than the host. Our main focus is the interplay between the coordination geometry and the so-called coordination chemistry at the impurity sites. The latter extends to the deviations in orbital occupation in the vicinity of the impurity, charge mobility, and possible leakage from the impurity site, and, consequently, the impurity charge state.

2. Materials and Methods

2.1. *Ab Initio* Method in Doped Systems

A general scheme to investigate the defect environment via theoretical and computational approaches consists of a supercell modeling in order to reach an adequate defect dilution. The substitutional doping is a regular impurity defect in this context and can be treated similarly [13]. One should be aware, though, that an introduction of a guest atom can drive other anomalies to arise, mostly in its vicinity (e.g., charge trapping, structural modifications, vacancies at nearest atomic positions). As hyperfine interactions at the dopant site are extremely sensitive to the variations in its immediate environment, their characteristics can be used as a reference for identification of the additional effects at this site. Thus, by simulating the most likely dopant-coupled defects and comparing the obtained hyperfine parameters, among which is the EFG tensor, with their experimental analogues, one can achieve a precise description of local effects induced by the guest atom.

The EFG tensor at the nucleus of an atom may be calculated directly from the full Coulomb-potential within the framework of the APW+lo (augmented plane waves + local orbitals) scheme [14]. Several DFT software packages offer APW+lo basis sets and/or derivatives, including the WIEN93 – 2k_21 series [15], favored by the hyperfine interactions community for the analysis of the oxide systems. The details of the simulation procedure can be found elsewhere [16,17]. Although we omit an explicit description of the method here, we emphasize the importance of the all-electron approach to obtain accurate values of the hyperfine parameters.

Two aspects of substitutional doping will be given priority in this review: (i) associated structural relaxations and (ii) the charge state of the impurity. To address (i), preliminary calculations are usually performed for an unrelaxed supercell, where the crystallographic data, including lattice parameters and atomic positions, commonly taken from powder diffraction studies, is kept fixed. In the main simulation, the supercell structure is optimized to ensure that the atomic positions are fully relaxed until Hellmann–Feynman forces on atoms are less than the chosen threshold value.

Concerning (ii), heterovalent doping is expected to affect the charge distribution in the host matrix, allowing an unbalanced local charge to arise near the impurity center by being captured into hydrogen-like orbitals.

In the selected oxide studies, the variation of the charge state of an impurity is treated as follows: an electron fraction may be added to (removed from) the supercell and compensated with a uniformly smeared charge of the same magnitude and opposite sign, the so-called background. The charge state at the site of dopant X is commonly denoted as $[X^{n\pm}]$, where n is the fraction of elementary negative charge e^- added to (“−” sign) or removed from (“+” sign) the impurity. The cell and the state are said to be neutral when no electrons are added or removed, which is denoted by $[X^0]$. This is a likely scenario for isovalent doping. For heterovalent doping, the maximal number of added (removed) electrons in a first-principles study usually reaches the difference in valence between the solvent and solute ions, with a one e^- step. For example, for a binary compound with a bivalent non-metallic element A, $M_2^{n_M+}A_{n_M}^{2-}$, one may consider an acceptor impurity $X^{n_X+}@M$, $n_X < n_M$, in the states $[X^{(n_M-n_X)-}]$, $[X^{(n_M-n_X-1)-}]$, \dots , $[X^0]$, correspondent to the addition of $n_M - n_X$, $n_M - n_X - 1$, \dots , 0 electrons to the system. For donor impurities with $n_X > n_M$, the electrons are removed, leading to $[X^0]$, $[X^{1+}]$, \dots , $[X^{(n_X-n_M)+}]$ states. Fractional charge steps are possible, albeit scarce in the literature due to a greater number of valence states to be considered and a consequent rise in computational costs.

As mentioned above, the hyperfine parameters at the impurity will depend on the distribution of the precipitated charge (if any) between the orbitals, the shape, and spatial orientation of the latter. Moreover, there is an interplay between the charge of the impurity and structure modifications in the immediate environment of the dopant. Thus, the hyperfine parameters obtained for relaxed and unrelaxed systems and different charge states of the impurity atoms may be compared to the experimental data to check the validity of simulated dopant-induced modifications in atomic structure and charge distribution. As a result, the nature of the electronic contribution to hyperfine interactions may be established, and the position of impurity bands, orbital hybridization, and other electronic properties may be described.

2.2. Details of Ab Initio Calculations in Oxides

For doped oxides, a supercell is constructed by unfolding the lattice parameters a , b , and c n_1 , n_2 , and n_3 times, respectively; thus, the supercell is denoted as $n_1 \times n_2 \times n_3$. When the unit cell contains a relatively large number of atoms, as in the case of bixbyites, $n_1 = n_2 = n_3 = 1$ is sufficient for an adequate dilution of the dopant. Thus, 1:32 (3.125 at.%) [5,7,8,10] and 1:16 (6.25 at.%) [4,18] dopant concentrations are usually considered for these trivalent metal oxides.

Local density (LDA), generalized gradient approximation (GGA), and Wu–Cohen GGA were most commonly employed to take account of exchange and correlation effects. Muffin-tin sphere radii of Cd usually varied from 1.02 to 1.11 Å, that of Ta was near 1 Å, and 0.85–0.97 Å were assigned to O. The size of the basis set in bixbyites was preferably restricted by $RK_{\max} = 7$, k -mesh density varied from 50 to 200 points in the full Brillouin zone. The typical tolerance value for the forces acting on the relaxed atoms was 0.025 eV/Å, but was chosen as small as 0.005 in particular cases (see, e.g., [19]).

The question of whether or not the considered M_2O_3 system tends to charge compensation at the impurity site was treated as follows: for Cd doping, two cases are usually considered, including neutral $[Cd^0]$ [5,18] and $[Cd^-]$ [8,9,18], i.e., an imitation of the situation when the system provides the lacking electron. In the latter case, a homogeneous positive background is added, as discussed in Section 2.1. For Ta, three possibilities were approached, including $[Ta^+]$ and $[Ta^{2+}]$, to which a negative background is adjusted, in addition to the neutral cell [4,7,9,10].

3. Results and Discussion

3.1. Cd Doping in TiO₂, SnO₂, CeO₂, ZnO, and SnO

In this section, we discuss the electric field gradient at Cd impurity (dopant) in few examples of transition metal oxides (TiO₂ and ZnO), rare-earth oxide (CeO₂), and *sp*-element oxides (SnO and SnO₂). Titanium dioxide (TiO₂) crystallizes in three possible structures: tetragonal rutile (space group $P4_2/mnm$), tetragonal anatase (space group $I4_1/amd$), and brookite with an orthorhombic structure (space group $Pbca$). The rutile phase presents octahedral coordination with six oxygen atoms as nearest neighbors (NN). Recent experimental TDPAC investigation of the EFG in the rutile phase of TiO₂ was carried out using ^{111m}Cd(¹¹¹Cd), ¹¹¹In(¹¹¹Cd), and ¹⁸¹Hf(¹⁸¹Ta) probe nuclei implanted into samples [20,21]. Although the probe nuclei were the same, different results were observed for ^{111m}Cd and ¹¹¹In generators. ¹¹¹In-generated Cd probes occupied a single site fraction in the rutile phase with $V_{zz} = 50.7 \text{ V}/\text{\AA}^2$ and $\eta = 0.18$, whereas ^{111m}Cd-generated probes were observed to populate two site fractions, the minor with V_{zz} similar to the previous one, but with a smaller asymmetry parameter $\eta = 0.15$, and $V_{zz} = 62.3 \text{ V}/\text{\AA}^2$ and $\eta = 0.79$ for the major fraction [20]. First-principles calculations using density functional theory performed on a supercell of TiO₂ with one Cd at substitutional Ti sites yield $V_{zz} = 45.5 \text{ V}/\text{\AA}^2$ and $\eta = 0.26$ at the Cd site for the [Cd²⁻] charge state, which differ slightly from the above experimental values and those reported by Schell et al. [21], all measured at 295 K (see Table 1).

Table 1. Experimental and theoretical values of V_{zz} and η at Cd sites, along with crystal properties of some Cd-doped oxides. Experimental V_{zz} values at room temperature were calculated considering $Q = 0.83$ b for ^{111}Cd .

Oxide	Experimental		Theoretical		Crystalline Structure			Ref.	
	$V_{zz}, \text{V}/\text{\AA}^2$	η	$V_{zz}, \text{V}/\text{\AA}^2$	η	Charge State	Space Group	Lattice Parameters $d_{\text{Cd-O}}, \text{\AA}^2$		
TiO ₂	50.7 ^a	0.18 ^a	45.5 ^d	0.26 ^d	[Cd ²⁻]	$P4_2/mnm$	$a = b = 4.653,$ $c = 2.969$	Cd-O1 = 2.18 Cd-O2 = 2.11	^a [20]
	55.74 ^b	0.12 ^b							^b [21]
	52.3 ^c	0.18 ^c							^c [22]
									^d [23]
SnO ₂	56.8 ^e	0.13 ^e	54.3 ^e	0.14 ^e	[Cd ²⁻]	$P4_2/mnm$	$a = b = 4.737,$ $c = 3.186$	Cd-O1 = 2.16 Cd-O2 = 2.20	^e [11]
	57.3 ^f	0.1 ^f	51.1 ^e	0.36 ^e	[Cd ⁰]				^f [24]
	48.2 ^g	0.15 ^g							^g [25]
	45.0 ^h	0.37 ^h							^h [26]
	56–63 ^{i,*}	0.42–0.18 ^{i,*}							ⁱ [27]
	58.3 ^j	0.18 ^j							^j [28]
	57.8 ^l	0.1 ^l							^l [29]
SnO	57.0 ^m	0.2 ^m	62.0 ⁿ	0.0 ⁿ	[Cd ⁰]	$P4/nmm$	$a = b = 3.799,$ $c = 4.841$	Cd-O = 2.26	^m [30]
	~53.0 ^o	~0.2 ^o	53.0 ^o	0.0 ^o	[Cd ⁰]				ⁿ [2] ^o [31]
ZnO	15.5 ^p	0.0 ^p	16.8 ^s	0.0 ^s	[Cd ⁰]	$P6_3mc$	$a = b = 3.289,$ $c = 5.307$	Cd-O = 2.21	^p [32]
	15.7 ^{q,r}	0.0 ^{q,r}							^q [33]
	16.0 ^s	0.09 ^s							^r [34] ^s [3]
CeO ₂ , monovacancy	26.4 ^t	0.1 ^t	27.6 ^t	0.0 ^t	[Cd ⁰]	$Fm\bar{3}m$	$a = 5.41$	Cd-O = 2.36	^t [12]
	26.5 ^u	0.0 ^u							^u [35]
CeO ₂ , divacancy	30.4 ^t	0.4 ^t	−31.5 ^t	0.37 ^t	[Cd ²⁺]				
	29.6 ^u	0.35 ^u							

* SnO₂ doped with 1.4 at.% Cd, range of values for measurements at RT after annealing in the range 670–970 K.

When measurements were performed at 823 K, however, the obtained values, $V_{zz} = 46.0 \text{ V}/\text{\AA}^2$ and $\eta = 0.21$, were much closer to the theory [21]. When the temperature rises, the crystal structure relaxes, lowering tensions in the sample lattice and thus approaching the simulated model from which the calculations for the relaxed lattice were taken. As DFT calculations imply 0 K, any deviation can be attributed to temperature differences.

Tin dioxide (SnO_2) crystallizes in the rutile structure with space group $P4_2/mnm$. Table 1 displays several results for EFG parameters obtained by TDPAC measurements with $^{111}\text{In}(^{111}\text{Cd})$. The values of V_{zz} range from $\sim 4 \text{ V}/\text{\AA}^2$ to $\sim 76 \text{ V}/\text{\AA}^2$, and the values of η are in the 0.1–0.6 range. Darriba et al. investigated Cd impurity in SnO_2 in depth using experimental TDPAC and comprehensive first-principles calculations with charge states ranging from $[\text{Cd}^0]$ to $[\text{Cd}^{2-}]$ [11]. The calculations showed that the p -electrons contribution to V_{zz} is dominant and nearly constant in this range, whereas the d -electrons contribution varies significantly, dictating how V_{zz} behaves with charge state. Schell et al. reported different values of EFG parameters, $V_{zz} \sim 45 \text{ V}/\text{\AA}^2$ and $\eta = 0.37$, for measurements at room temperature (RT) in SnO_2 thin films after a 10 min annealing at $600 \text{ }^\circ\text{C}$ [26]. Interestingly, these values roughly agree with those obtained by first-principles calculations for $[\text{Cd}^0]$ (see Table 1). Schell et al. investigated the hyperfine interactions at $^{111}\text{In}(^{111}\text{Cd})$ in SnO_2 doped with 1.4 at.% Cd. The results obtained at RT after annealing at temperatures between 673 K and 973 K showed that V_{zz} increases and η decreases with annealing temperature [27]. This behavior can explain the values of hyperfine parameters experimentally observed after a short annealing. As defects are not removed upon such treatment, they can affect the hyperfine interactions. Since the calculations showed that the hyperfine parameters of such samples can be associated with neutral impurity, we can presume that, as ^{111}Cd probes are the product of ^{111}In decay, the time window of TDPAC measurement was not sufficient for charge rebalance near the defects, and the measurements are taken in the neutral state.

Tin monoxide (SnO) crystallizes in the tetragonal structure with the $P4/nmm$ space group and lattice parameters $a = b = 3.7986 \text{ \AA}$ and $c = 4.8408 \text{ \AA}$. Each Sn atom is surrounded by four oxygen atoms in a prismatic tetragonal coordination. Theoretical hyperfine parameters were found to be $V_{zz} = 62.0 \text{ V}/\text{\AA}^2$ and $\eta = 0.0$ [2], and remained in good agreement with the experimental values of $V_{zz} = 57.0 \text{ V}/\text{\AA}^2$ and $\eta = 0.2$ [30]. Recently, hyperfine interactions in SnO were experimentally and theoretically investigated with the hyperfine parameters measured as a function of temperature by TDPAC using $^{111}\text{In}(^{111}\text{Cd})$ [31]. At room temperature, the reported values were $V_{zz} \sim 53.0 \text{ V}/\text{\AA}^2$ and $\eta = 0.2$. Calculations for neutral supercell yielded $V_{zz} = 53.0 \text{ V}/\text{\AA}^2$ and $\eta = 0.0$, in an excellent agreement with experimental values. Comprehensive calculations of V_{zz} as a function of charge state showed that the d -contribution is almost independent of charge state, so that the p -contribution determines V_{zz} behavior. Thus, the tendency is opposite to that in SnO_2 mentioned above, although in both oxides p -contribution is dominant.

Zinc monoxide (ZnO) crystallizes in the hexagonal structure with $P6_3mc$ space group and lattice parameters $a = b = 3.289 \text{ \AA}$, $c = 5.307 \text{ \AA}$, where the Zn atom presents a tetrahedral coordination with four oxygen atoms. Experimental values measured at room temperature revealed $V_{zz} \sim 16.0 \text{ V}/\text{\AA}^2$ and $\eta = 0.0$ [3,32–34]. Calculations considering neutral charge state of the impurity yielded $V_{zz} = 16.8 \text{ V}/\text{\AA}^2$ and $\eta = 0.0$ [3] and remained in excellent agreement with experimental values. Again, as DFT implies 0 K, a slight decrease of V_{zz} with temperature is not unexpected.

Cerium dioxide (CeO_2) crystallizes in the cubic structure (space group $Fm\bar{3}m$) with lattice parameter $a = 5.41 \text{ \AA}$, in which the Ce atom is surrounded by eight oxygen atoms. Due to the structure symmetry, it is expected that both V_{zz} and η vanish; however, TDPAC experiment with $^{111}\text{In}(^{111}\text{Cd})$ yielded non-zero hyperfine parameters. Wang et al. observed two different environments for the probes, characterized by $V_{zz} = 26.5 \text{ V}/\text{\AA}^2$ and $\eta = 0.0$ and $V_{zz} = 29.6 \text{ V}/\text{\AA}^2$ and $\eta = 0.35$, respectively [35]. Those were assumed to be due to oxygen vacancies. Ferreira et al. recently reported similar experimental values ($V_{zz} = 26.4 \text{ V}/\text{\AA}^2$ and $\eta = 0.1$ and $V_{zz} = 30.4 \text{ V}/\text{\AA}^2$ and $\eta = 0.4$) [12], and *ab initio* calculations were performed in order to characterize the oxygen vacancies perturbing the interaction. Theoretical

study yielded $V_{zz} = 27.6 \text{ V}/\text{\AA}^2$ and $\eta = 0.0$ for a single vacancy at the position of nearest neighbor oxygen atom in (111) plane and a neutral charge state of Cd impurity. Moreover, a simulation of two oxygen vacancies in (11 $\bar{1}$) and (111) planes gave $V_{zz} = 29.6 \text{ V}/\text{\AA}^2$ and $\eta = 0.35$ at $[\text{Cd}^{2-}]$ impurity. Both theoretical results agree very well with the experimental ones. Furthermore, Wang et al. reported a third quadrupole interaction for a fraction of $^{111}\text{In}(^{111}\text{Cd})$ probes characterized by $V_{zz} = 130 \text{ V}/\text{\AA}^2$ and $\eta = 0.0$, which matches with the simulation of two oxygen vacancies in (11 $\bar{1}$) and ($\bar{1}\bar{1}1$) calculated for $[\text{Cd}^{2+}]$ resulting in $V_{zz} = 120 \text{ V}/\text{\AA}^2$ and $\eta = 0.01$ [12].

The hyperfine parameter results for the five Cd-doped semiconductor oxides shown in Table 1 highlight remarkable aspects of the complementary method of TDPAC plus first-principles calculations for doping investigation. Once again, we emphasize that the goal here is not to focus on the doping effect on the macroscopic properties of semiconductor oxides, but rather to investigate the electronic structure in the vicinity of the dopant, which is the source of the changes in the macroscopic properties.

When Cd atoms with valence +2 replace the cations in the monoxide, such as Zn and Sn (in SnO), the best agreement of hyperfine parameters is obtained from calculations with neutral charge state of the impurity. For Cd replacing tetravalent cations (Sn in SnO₂ and Ti in TiO₂), the agreement is best when the calculations are performed with two electrons added to the supercell ($[\text{Cd}^{2-}]$ charge state). The case of CeO₂, where Ce ion is also tetravalent, stands out though. Despite the cubic structure, which would result in vanishing hyperfine parameters, non-zero parameters were observed experimentally, which was attributed to oxygen vacancies in the vicinity of Cd impurity. Considering one oxygen vacancy, the agreement of hyperfine parameters with experimental values is obtained when calculations are performed for a neutral cell, despite the difference between the valences of Ce⁴⁺ and Cd²⁺. In the case of two oxygen vacancies, the agreement of the results with experiment is achieved only upon a removal of two electrons ($[\text{Cd}^{2+}]$). Because of the difference in valences of Ce⁴⁺ and Cd²⁺, the vacancy at the position of a single O²⁻ ion eliminates the need for charge compensation. When two oxygen ions are missing, however, the agreement between calculations and experimental results indicates that two electrons must be removed to compensate for the charge difference. The results of juxtaposition of theoretical and experimental data described above confirm that TDPAC is very sensitive to electronic charge (number of electrons) and structure (electron (de)-localization), which may be affected by the defects in the probe's vicinity such as oxygen vacancies.

3.2. Doping in M₂O₃, M = Sc, Y, In

In this review we consider Sc₂O₃, Y₂O₃, and In₂O₃ crystallized in *Ia3* bixbyite-type structure with lattice parameters of 10.1, 10.6, and 10.12 Å respectively [36–38]. This structure reveals two types of crystallographic sites occupied by metal cations M, commonly referred to as C and D sites, with nominal relative fraction $f(C)/f(D) = 3:1$. The geometries of both C and D may be treated as distorted octahedra formed by six O atoms around M. There are three distinct bond pairs connecting M@C to nearest neighbor oxygen (O_{NN}), whereas all six M@D–O_{NN} bonds are equal in length. An intuitive guess based on the geometry of (M@C)O₆ and (M@D)O₆ would be $0 \approx \eta^D < \eta^C$.

Concerning the hyperfine parameters measured with TDPAC in M₂O₃, although there was some controversy in their interpretation, the experimental values of V_{zz} and η showed a very high degree of reproducibility. This is remarkable considering the diversity of the sample preparation methods and measurement conditions, as well as different techniques used for probe incorporation. The generalization of TDPAC results for V_{zz} and η in M₂O₃ (M = Sc, Y, In) is presented in Table 2. Here, we call the reader's attention to the updated value of cadmium-111 nuclear quadrupole moment used for V_{zz} extraction from experimental data, $Q(5/2^+) = 0.664 \text{ b}$ [39], which is 20% less than the most commonly used $Q(5/2^+) = 0.83 \text{ b}$. Thus, the presented V_{zz} values are 25% higher than in the majority of comparative DFT+TDPAC studies for M₂O₃. Thus, an agreement between TDPAC and *ab initio* V_{zz} values claimed to be excellent by the authors of the herein reviewed works

may actually conceal up to 25% discrepancy. As one can see with the help of Table 2, experiments yield the expected relation $\eta^D < \eta^C$ for all the probes.

In what follows, we focus on structure relaxations induced by Cd and Ta doping in bixbyite matrices, especially the modifications in coordination geometry of M and O_{NN} atoms, as well as on the rearrangement of charge density in the vicinity of the dopant nucleus, and how these effects influence the hyperfine parameters.

Table 2. The main component of EFG tensor and asymmetry obtained with TDPAC (in bold) and DFT for assigned C and D sites of chosen bixbyites. To calculate V_{zz} from experimental data, we used the following values of nuclear quadrupole moments: $Q(^{111}\text{Cd}, 5/2^+) = 0.664$ b [39], $Q(^{181}\text{Ta}, 5/2^+) = 2.36$ b [40], and $Q(^{44}\text{Sc}, 1^+) = 0.214$ b [41]. Only well-defined reliable experimental data unambiguously attributed to C and D sites by the authors of cited works were employed in averaging.

Compound	Impurity	$d_{M-O}^C, \text{Å}$	$d_{M-O}^D, \text{Å}$	$V_{zz}^C, \text{V/Å}^2$	η^C	$V_{zz}^D, \text{V/Å}^2$	η^D	Ref.
Sc ₂ O ₃	–	2.08/2.12/2.16	2.12	–29.6	0.69	45.8	0	[19]
	⁴⁴ Sc			27.8 ± 0.4	0.63	42.6 ± 0.7	0	[19,42]
	¹¹¹ Cd			82.2 ± 0.2	0.71 ± 0.01	103.3 ± 0.5	0	[1,6]
	[Cd [–]]	2.08/2.12/2.16	2.12	–49.1	0.65	86.5	0	
	[Cd [–]]	2.17/2.30/2.31	2.28	67.5	0.74	80.5	0	[5]
	¹⁸¹ Ta			141.2	1	178.6	0.16	[43]
	[Ta ⁰]	2.00/2.04/2.11	2.08	127.2	0.82	90	0	
[Ta ⁺]	1.98/2.01/2.09	2.04	–167.5	0.45	165	0	[7]	
[Ta ²⁺]	1.97/1.99/2.06	2.00	–183	0.18	273	0		
Y ₂ O ₃	¹¹¹ Cd			53.1 ± 1.6	0.79 ± 0.02	92.4 ± 0.8	0	[1,44]
	¹⁸¹ Ta			133.1 ± 3.3	0.54	237.0 ± 6.4	0.07	[4,45,46]
	[Ta ⁰]			–115.4	0.65	–99.6	0	
	[Ta ⁺]	2.24/2.27/2.33	2.28	–189	0.44	–27.8	0	
	[Ta ²⁺]			–151.3	0.66	236.2	0	
	[Ta ⁰]	1.99/2.07/2.16	2.13	57.2	0.65	50.3	0	[4]
	[Ta ⁺]	1.99/2.03/2.15	2.07	–76.5	0.71	147.1	0	
[Ta ²⁺]	1.98/2.01/2.11	2.03	–137.1	0.60	259.4	0		
In ₂ O ₃	–	2.13/2.19/2.23	2.18	54	0.98	82	0	[8]
	¹¹¹ Cd			73.3 ± 1.0	0.72 ± 0.02	96.1 ± 1.3	0.10 ± 0.09	[1,18,47–55]
	[Cd ⁰]	relaxed		–30.8	0.01	71.5	0	[18]
	[Cd [–]]	2.13/2.19/2.23	2.18	48	0.96	78	0	
	[Cd [–]]	2.20/2.29/2.33	2.27	56	0.68	76	0	[8]
	¹⁸¹ Ta			150.7 ± 19.3	0.37 ± 0.18	172.1 ± 12.4	0.09 ± 0.06	[10,56,57] *
	[Ta ⁰]	1.95/1.95/2.12	2.02	–174	0.13	199	0	
[Ta ⁺]	1.95/1.96/2.13	2.00	–175	0.12	209	0	[10]	
[Ta ²⁺]	1.96/1.96/2.13	2.01	–174	0.10	208	0		

* We performed the swap of site assignment given in [57] in accordance with most recent and explicit study [10].

3.2.1. Coordination Geometry of the Dopant

The relaxation of lattice parameter in the self-consistent simulation loop for the case of 6.25 at.% Fe, Co, Ni doping in In₂O₃ led to its maximal correction of ~0.8% that remained in agreement with ~0.4%, found with X-ray diffraction in the same study, and had negligible dependence on the site occupied by the dopant [18]. As the absolute difference between the solute and the solvent ionic radii in sixfold coordination for Fe, Co, Ni (18.8–31.3%) is similar to those of Cd and Ta (18.8 and 20%, respectively) [58], one should expect a comparable effect of Cd and Ta doping on the host lattice. On the other hand, the relaxation of atomic positions was shown to induce noticeable onsite Cd/Ta–O_{NN} bond extensions/contractions of 3.3–4.6%/4.5–10.5% (at site C) and 4.1%/7.8% (at site D) [8–10]. At both sites C and D, Ta induces greater distortions than Cd, which correlates with aforementioned deviations of dopant ionic radii from that of the host cation. According to Errico et al., the hyperfine parameters at site C exhibited sensitivity to such

modifications in its geometry. For $\text{In}_2\text{O}_3:\text{Cd@C}$, V_{zz} increased by 16.7%, whereas the asymmetry decreased by a drastic 29.2% [8,9]. Site D was affected much milder, demonstrating a 2.6% reduction of V_{zz} and preserved symmetry. The positions of atoms other than those in the closest vicinity to the impurity remained almost unaffected. This may result in an assumption about the essential role of the NN O atoms in the charge distribution around the dopant nucleus, at least at the C site.

The probe-induced rearrangement of nearest oxygen atoms in In_2O_3 was already mentioned in earlier works [56], and was further interpreted as a tendency to the reconstruction of the local environment of Cd or Ta in their native oxides [9,10]. However, the quantitative discussion was restricted to the comparison of M–O_{NN} bond lengths in the distorted sites and Cd/Ta native oxides. For the juxtaposition of Cd in CdO and at the symmetric D-site, this argumentation is sufficient, but other cases may not be that evident. We note here that the sixfold coordinated Cd in its stable oxide CdO ($Fm\bar{3}m$) is a center of a regular octahedron, implying vanishing V_{zz} and η . Ta_2O_5 , naturally favoring an amorphous state, has several allotropes, including the most common low-temperature β ($Pccm$) and high-temperature α ($I2$) phases [59,60], with a continuing debate on the details of their structures. According to [59,60], β - Ta_2O_5 has two distinct TaO_6 geometries, which we refer to as β_S and β_A , whereas α - Ta_2O_5 has only one sixfold coordinated site (to be referred to as α_A in what follows); all sites are shown in Figure 1.

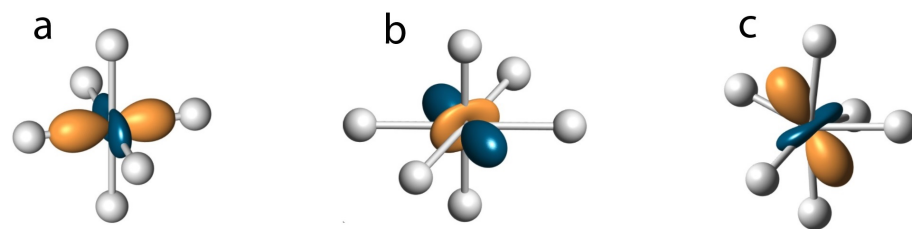


Figure 1. Sixfold coordinated Ta sites in Ta_2O_5 : (a) β_S and (b) β_A of β - Ta_2O_5 ; (c) α_A of α - Ta_2O_5 [59,60]. EFG produced by NN within the ionic model is shown, tensor visualization strategy was adopted from [61], orange is used for positive and teal for negative components.

Unlike that of CdO, the geometries of these sites do not allow immediate conclusions on associated hyperfine parameters, and, to our knowledge, appropriate experimental data are lacking. For $\text{In}_2\text{O}_3:\text{Ta}$, this hinders the comprehension of the qualitative comparison presented in [9,10]. Furthermore, for $M = \text{Cd}, \text{Ta}$ at site C of In_2O_3 , M–O bond length transformations were found to be anisotropic. As shown in Table 2 and Figure 2, there is no evident tendency for bond length uniformization that could allow a guess on the drop of η and/or V_{zz} . In this regard, for the quantitative estimation of dopant-induced distortion at C-site, we adopt the algebraic part of EFG tensor (i.e., with physical constants omitted) calculated for the immediate cation environment within the point charge model (PCM), given by

$$v_{NN}^{ij} = -2 \sum_{n=1}^6 \frac{r_n^2 \delta^{ij} - 3x_n^i x_n^j}{r_n^5}, \quad (1)$$

where $\vec{r}_n = (x_n^1, x_n^2, x_n^3)$ denotes the position of the n -th oxygen ion relative to central cation. For the introduced tensor, one may calculate η_{NN} , an analogue of the hyperfine asymmetry parameter η . The effect of O_{NN} position's relaxation on v_{NN}^{ij} is revealed with the help of Figure 2.

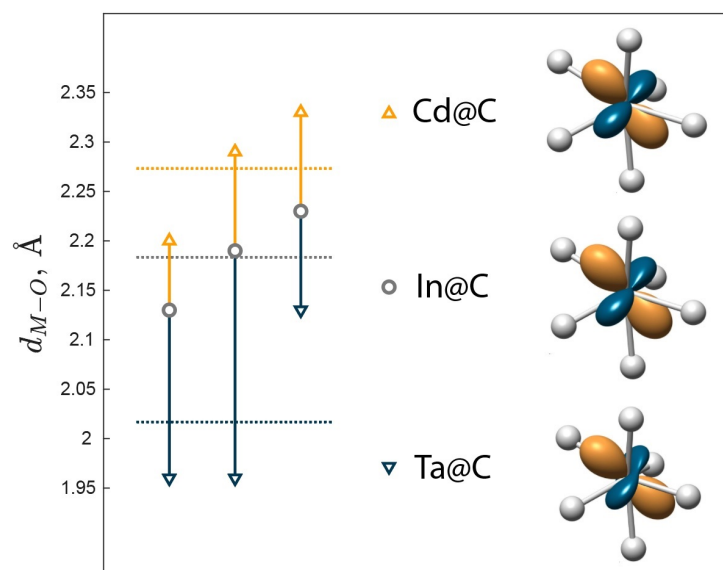


Figure 2. DFT-predicted M@C–O_{NN} bond length modulation for M = Cd, Ta [8,10] (left) and the EFG tensor of the immediate environment calculated within PCM (right). Bond direction and central cation position alterations upon relaxation were neglected.

Both Cd and Ta leave the v_{NN} major component in (M@C)O₆ octahedron almost unchanged; although Cd induces a greater reduction in it, the difference does not exceed 5%. The rotation of basis vectors is minor, if any. Bond length modulation affects tensor asymmetry though, allowing a 19.3% increase and a 45.9% decrease for Cd@C and Ta@C, respectively. The lobes correspondent to negative and positive components of v_{ij} shown in Figure 2 become almost equal due to Cd substitution, whereas for Ta@C the negative lobe becomes more similar to a torus around the positive lobe. Considering the significant v_{NN} asymmetry of unperturbed (In@C)O₆, further skewing induced by the substitution of In with Cd and consequent O position relaxation makes it less similar to the regular CdO₆ in CdO. In contrast, the symmetrization occurring for Ta@C drags the parameters closer to those of the β_S or α_A site of Ta₂O₅. Evidently, (In@D)O₆ preserves coordination symmetry upon the cation swap, but suffers the changes in the principal component of v_{NN} by –13.8 and 24.2% for M = Cd and Ta, as expected upon the respective extension and contraction of bond distances. Interestingly, when parametrized with (1), the geometry of (Ta@D)O₆ upon relaxation resembles that of β_A in Ta₂O₅. Thus, parametrizing the immediate environment with (1) we can confirm the reconstruction of native oxide declared in [9] for (Cd, Ta)@D and Ta@C but not for Cd@C.

Similarly to In₂O₃:Cd, *ab initio* analysis showed that the lattice parameter of Sc₂O₃:Cd varies less than 1% upon structure relaxation [5]. The optimized positions of oxygen atoms in the immediate environment of dopant, either Cd or Ta, are shifted with respect to the original XRD data obtained for pure samples [5,7]. Again, as in the case of In₂O₃:(Cd/Ta), those shifts are anisotropic for (Cd/Ta)@C and vary from 4.3/3.2 to 8.5/5.2%, whereas the (Cd/Ta)@D–O_{NN} bonds are equally extended/contracted by 7.5/3.8%. The effects of Cd and Ta on scandia matrix show, therefore, a tendency opposite to that observed in In₂O₃. Namely, on average, Cd induces greater perturbations to the impurity environment in Sc₂O₃ than Ta. The relaxation of atomic positions in Y₂O₃:Ta was shown to drive (Ta@C)–O_{NN} contractions of up to 11.6% and (Ta@D)–O_{NN} contractions of nearly 11%, which are greater than those in (In, Sc)₂O₃:Ta [4]. The relative effect of Cd and Ta doping on indium, scandium, and yttrium oxides is not unexpected and correlates with the relation between the ionic radii of these elements in sixfold coordination: $R(\text{Ta}) < R(\text{Sc}) < R(\text{In}) < R(\text{Y}) < R(\text{Cd})$.

Characterization of (Sc,Y)₂O₃:(Cd,Ta) with v_{NN}^{ij} of (1) showed that the asymmetry of the immediate cation environment remains practically unchanged upon doping. The only noticeable effect on η_{NN} was observed for Sc₂O₃:Cd@C, where it increased by almost 30%.

As in the case of In_2O_3 , Cd ion does not tend to reconstruct a symmetric cubic CdO-like environment at site C of Sc_2O_3 . The behavior of the major components of v_{NN}^{ij} of yttria and scandia, in principle, is consistent with the induced alterations of dopant–oxygen bond lengths; their absolute values decrease upon bond extension and increase upon contraction. Comparing the results obtained for Sc_2O_3 , Y_2O_3 , and In_2O_3 , one may conclude that site C of In_2O_3 is the most responsive, at the local level and in terms of η_{NN} , to the inclusion of impurities. This somewhat correlates with the experimental data shown in Table 2.

It is clear that, with an access to *ab initio* theoretical analysis, PCM was discredited as a tool to simulate hyperfine parameters. However, we still see some perspectives in its adoption at a conceptual level, as it is expected to help avoid ambiguities, e.g., in the characterization of site geometry.

3.2.2. Coordination Chemistry and Hyperfine Parameters

Comparing the results presented for $\text{In}_2\text{O}_3:\text{[Cd}^0\text{]}$ [18] with those for $\text{In}_2\text{O}_3:\text{[Cd}^-\text{]}$ [8,18] (in both states the atomic positions were relaxed), one can easily notice the difference in hyperfine parameters for Cd@C. The asymmetry changes from 0.01 in the neutral cell to 0.72 for the charged state [18]. The major component of the EFG tensor, besides increasing by almost 86% in absolute value, changes its sign upon the electron addition. Since the data obtained for $\text{In}_2\text{O}_3:\text{[Cd}^-\text{]@C}$ correlate better with the experiment, the partial negative charge was assumed to be smeared near the impurity in the real system. Similar to $\text{SnO}_2:\text{Cd}$ [11], charge localization along M–O bonds, i.e., the change in the occupancy of nearest neighbor O *p* orbitals, and the variation of the occupancy of Cd *d* orbitals may be responsible for the observed perturbation of the hyperfine parameters. The hyperfine parameters at site D remain almost unaffected by the charge state of Cd impurity, and both $[\text{Cd}^0]$ and $[\text{Cd}^-]$ calculations give the predictions that agree well with experimental data. Although such similarity hinders the identification of the charge state of the probe at site D, Sena et al. argue for $[\text{Cd}^-]$ [18]. The difference in the way the hyperfine parameters are affected by the charge state of Cd@C and Cd@D may be connected with the relative orientation of NN oxygen *p* orbitals and Cd *d* orbitals at C and D sites.

When In atom at either C or D site is substituted by a donor Ta, the alteration of the charge state of the impurity from 0 to 2+ leaves the hyperfine parameters practically intact, and the DFT predictions are close to their experimental values. Richard et al. determined that only 4% of the added partial $2|e|$ positive charge in $\text{In}_2\text{O}_3:\text{[Ta}^{2+}\text{]}$ precipitates within the 1 Å radius sphere around the Ta nucleus, whereas its greatest portion of 75% is distributed among the NN oxygen [10]. Moreover, the distribution of the additional charge in the vicinity of the Ta nucleus was found to be almost spherical. However, a complementary analysis of the defect-formation energy allowed us to conclude on the superior stability of the double-charged impurity for $\text{In}_2\text{O}_3:\text{Ta}$.

In contrast to $\text{In}_2\text{O}_3:\text{Ta}$, for Ta-doped yttria, the hyperfine parameters varied significantly upon the impurity charge, and their best resemblance to experimental analogues was obtained when the impurity reached 2+ state [4]. According to Richard et al. in the case of completely ionized impurity, 20% of the two electrons removed from the cell were extracted from the 1 Å sphere around Ta nuclei. The major component of the EFG tensor was, to a greater extent, defined by the contribution of Ta *p* orbitals for both Ta@C and Ta@D. Its perturbation, associated with the population of Ta 5*d* orbitals, was found to be critical for the neutral cell and $\text{Y}_2\text{O}_3:\text{[Ta}^+\text{]}$, but became less than 10% (Ta@C) and 5% (Ta@D) for $\text{Y}_2\text{O}_3:\text{[Ta}^{2+}\text{]}$. It is worth noting here that the removal of $1e^-$ and $2e^-$ affects different sets of M@C– O_{NN} bonds. As emphasized by Darriba et al., this may be the result of Coulomb repulsion acting on one of the partial positive charges by the other, and its consequent preference for an alternative distribution geometry in space [11]. Hence, this may cause a compensation effect in the vicinity of Ta nucleus, so that the resulting distribution of the removed charge is nearly spherical.

An *ab initio* study of pure Sc_2O_3 allowed to establish the dominance of Sc *p*-orbitals contribution to the major EFG component at both sites C (94.9%) and D (91.6%) [19]. The *d*-

orbitals form only 5.5 and 8% part of V_{zz} , respectively. This agrees with the predictions of Blaha et al., who argued for the dominance of p contribution due to the proximity of the nodes of p wave functions to metallic nuclei [62].

For acceptor impurities in scandia, the comparison of DFT-based predictions for hyperfine parameters with their experimental analogues resulted in the conclusion on the impurity charge state; namely, it indicated the impurity ionization, $\text{Sc}_2\text{O}_3:[\text{Cd}^-]$ [5].

A similar, but more detailed, analysis was presented for donor Ta in Sc_2O_3 matrix by Richard et al. [7]. The difference in electron content within 1.9 Å around the Ta nucleus for $[\text{Ta}^0]$ and $[\text{Ta}^{2+}]$ systems was 0.4 and 0.6 electrons for sites C and D, respectively, i.e., the introduced partially positive charge precipitates more effectively at the symmetric site. The hyperfine parameters were found to change drastically upon electron removal for both Ta@C and Ta@D. The hyperfine parameters associated with site C suffered moderate changes upon the removal of the second electron; hence, it was assumed delocalized. Generally, EFG values obtained for the $\text{Sc}_2\text{O}_3:[\text{Ta}^+]$ system showed a greater degree of coincidence with experimental data.

4. Conclusions

In this review we examined the efficiency of TDPAC and *ab initio* calculations combination for studying doping-induced local effects in bi-, tri-, and tetravalent semiconductor oxides. The combination proved itself productive, as high correlation between theoretical predictions and experimental data was achieved in most cases. Such concordance, when exists, grants the validity of the specific assumptions employed in DFT-based analysis for the real system. For the materials employed in this review, the combination of experimental and theoretical data allowed to distinguish several major trends. First, the system tends to feed the impurity site with an appropriate amount of charge that compensates the difference in valence between the dopant and indigenous ions. However, this compensating charge does not precipitate fully in the muffin-tin sphere of the dopant and is partially (sometimes in the most part) delocalized on the neighboring atoms. The compensation trend extends to the cases of impurity-coupled defects such as oxygen vacancies. The deviations from this trend for $^{111}\text{In}(^{111}\text{Cd})$ can be explained by external effects that slow charge rebalance. Second, independently of the charge state, p -orbitals produce dominant contribution to the major component of EFG tensor, as expected due to their shape. At the same time, d contribution may vary significantly upon charge state, and such variation may drastically perturb the hyperfine parameters, especially the asymmetry of EFG. Additionally, the more symmetric the immediate environment of the impurity site, the less the associated hyperfine parameters would be affected by its charge state. As for the structural properties, dopant does not seem to cause appreciable modulations other than in its closest proximity. The intensity of cation substitution effect on $\text{M}-\text{O}_{\text{NN}}$ bond lengths correlates well with the relation of the radii of host and guest ions. On the other hand, the tendency for the dopant to reconstruct the site symmetry of its native oxides does not necessarily govern the relaxation pattern. Finally, we showed that the simple ionic model, although assigned useless for adequate interpretation of TDPAC data, may be adopted to avoid conceptual ambiguities, e.g., in characterization of site asymmetry.

Author Contributions: Conceptualization, A.B. and A.W.C.; methodology, A.B., A.W.C. and W.L.F.; validation, A.B., A.W.C. and R.N.S.; formal analysis, A.B. and A.W.C.; investigation, A.B., A.W.C., N.P.d.L., A.A.M.F., A.P.d.S.S., T.d.S.N.S., W.L.F., L.F.D.P., B.S.C.; resources, A.W.C.; data curation, A.B.; writing—original draft preparation, A.B., A.W.C. and R.N.S.; writing—review and editing, A.B.; visualization, A.B.; supervision, A.W.C. and R.N.S.; project administration, A.B., A.W.C. and R.N.S.; funding acquisition, A.W.C. All authors have read and agreed to the published version of the manuscript.

Funding: A.B. and T.d.S.N.S. acknowledge the Instituto de Pesquisas Energéticas e Nucleares IPEN-CNEN for financial support, projects 2020.06.IPEN.43 and 2020.06.IPEN.38, respectively (2022/07); A.B. and A.W.C. acknowledge São Paulo Research Foundation (FAPESP) for grants # 2019/15620-0 and 2017/50332-0, 2018/18657-0, respectively; A.A.M.F. and W.L.F. acknowledge CAPES for personal grants 88887.661225/2022-00 and 88887513796/2020-00, respectively; A.P.d.S.S. was funded by CNEN under the grant 01341.005171/2021-60; N.P.d.L., B.S.C., R.N.S., and A.W.C. acknowledge CNPq for personal grants 140071/2020-2, 142070/2019-0, 303577/2018-5, and 307322/2021-1, respectively.

Acknowledgments: A.B. acknowledges the support of IPEN staff, especially F.A. Genezini and P.C.S. Silva.

Conflicts of Interest: The authors declare no conflict of interest.

References

1. Bartos, A.; Lieb, K.P.; Uhrmacher, M.; Wiarda, D. Refinement of Atomic Positions in Bixbyite Oxides using Perturbed Angular Correlation Spectroscopy. *Acta Cryst.* **1993**, *B49*, 165–169. [CrossRef]
2. Errico, L.A.; Rentería, M.; Petrilli, H.M. Cd in SnO: Probing structural effects on the electronic structure of doped oxide semiconductors through the electric field gradient at the Cd nucleus. *Phys. Rev. B* **2007**, *75*, 155209. [CrossRef]
3. Muñoz, E.L.; Mercurio, M.E.; Cordeiro, M.R.; Pereira, L.F.D.; Carbonari, A.W.; Rentería, M. Dynamic hyperfine interactions in $^{111}\text{In}(^{111}\text{Cd})$ -doped ZnO semiconductor: PAC results supported by *ab initio* calculations. *Phys. B* **2012**, *407*, 3121–3124. [CrossRef]
4. Richard, D.; Rentería, M.; Carbonari, A.W. Substitutional Ta-doping in Y_2O_3 semiconductor by sol-gel synthesis: Experimental and theoretical studies. *Semicond. Sci. Technol.* **2017**, *32*, 085010. [CrossRef]
5. Muñoz, E.L.; Richard, D.; Errico, L.A.; Rentería, M. *Ab initio* study of the EFG tensor at Cd impurities in Sc_2O_3 semiconductor. *Phys. B* **2009**, *404*, 2757–2759. [CrossRef]
6. Muñoz, E.L.; Richard, D.; Carbonari, A.W.; Errico, L.A.; Rentería, M. PAC study of dynamic hyperfine interactions at ^{111}In -doped Sc_2O_3 semiconductor and comparison with *ab initio* calculations. *Hyperfine Interact.* **2010**, *197*, 199–205. [CrossRef]
7. Richard, D.; Muñoz, E.L.; Errico, L.A.; Rentería, M. Electric-field gradients at Ta impurities in Sc_2O_3 semiconductor. *Phys. B* **2012**, *407*, 3134–3136. [CrossRef]
8. Errico, L.A.; Rentería, M.; Fabricius, G.; Darriba, G.N. FLAPW Study of the EFG Tensor at Cd Impurities in In_2O_3 . *Hyperfine Interact.* **2004**, *158*, 63–69. [CrossRef]
9. Errico, L.A.; Rentería, M.; Bibiloni, A.G.; Freitag, K. Nonionic contributions to the electric-field gradient at ^{181}Ta and ^{111}Cd impurity sites in R_2O_3 (R = Sc, In, Lu, Yb, Tm, Er, Y, Ho, Dy, Gd, Eu, Sm) bixbyites. *arXiv* **2005**. [CrossRef]
10. Richard, D.; Darriba, G.N.; Muñoz, E.L.; Errico, L.A.; Eversheim, P.D.; Rentería, M. Experimental and First-Principles Theoretical Study of Structural and Electronic Properties in Tantalum-Doped In_2O_3 Semiconductor: Finding a Definitive Hyperfine Interaction Assignment. *J. Phys. Chem. C* **2016**, *120*, 5640–5650. [CrossRef]
11. Darriba, G.N.; Muñoz, E.L.; Carbonari, A.W.; Rentería, M. Experimental TDPAC and Theoretical DFT Study of Structural, Electronic, and Hyperfine Properties in $(^{111}\text{In} \rightarrow)^{111}\text{Cd}$ -Doped SnO_2 Semiconductor: *Ab Initio* Modeling of the Electron-Capture-Decay After-Effects Phenomenon. *J. Phys. Chem. C* **2018**, *122*, 17423. [CrossRef]
12. Ferreira, W.L.; Pereira, L.F.D.; Leite Neto, O.F.S.; Maciel, L.S.; Gonçalves, V.C.; Saxena, R.N.; Carbonari, A.W.; Costa, M.S.; Cabrera-Pasca, G.A. Locally symmetric oxygen vacancy around Cd impurities in CeO_2 . *Phys. Rev. B* **2021**, *104*, 035146. [CrossRef]
13. Cottenier, S. *Density Functional Theory and the Family of (L)APW-Methods: A Step-by-Step Introduction*, 2nd ed.; Ghent University: Ghent, Belgium, 2013. Available online: http://www.wien2k.at/reg_user/textbooks/ (accessed on 10 August 2022).
14. Andersen, O.K. Linear methods in band theory. *Phys. Rev. B* **1975**, *12*, 3060. [CrossRef]
15. Blaha, P.; Schwarz, K.; Tran, F.; Laskowski, R.; Madsen, G.K.H.; Marks, L.D. WIEN2k: An APW+lo program for calculating the properties of solids. *J. Chem. Phys.* **2020**, *152*, 074101. [CrossRef]
16. Koch, K.; Cottenier, S. Analysis of an Electric-Field Gradient (EFG). Technical Report . 2011. Available online: http://www.wien2k.at/reg_user/faq/efg2.pdf (accessed on 10 August 2022).
17. Novák, P. Calculation of Hyperfine Field in WIEN2k. Technical Report. 2006. Available online: http://www.wien2k.at/reg_user/textbooks/Bhf_3.pdf (accessed on 10 August 2022).
18. Sena, C.; Costa, M.S.; Muñoz, E.L.; Cabrera-Pasca, G.A.; Pereira, L.F.D.; Mestnik-Filho, J.; Carbonari, A.W.; Coaquira, J.A.H. Charge distribution and hyperfine interactions in the vicinity of impurity sites in In_2O_3 doped with Fe, Co, and Ni. *J. Magn. Magn. Mater.* **2015**, *387*, 165–178. [CrossRef]
19. Richard, D.; Muñoz, E.L.; Butz, T.; Errico, L.A.; Rentería, M. Electronic and structural properties, and hyperfine interactions at Sc sites in the semiconductor Sc_2O_3 : TDPAC and *ab initio* study. *Phys. Rev. B* **2010**, *82*, 035206. [CrossRef]
20. Schell, J.; Lupascu, D.C.; Correia, J.G.M.; Carbonari, A.W.; Deicher, M.; Barbosa, M.B.; Mansano, R.D.; Johnston, K.; Ribeiro, I.S., Jr. In and Cd as defect traps in titanium dioxide. *Hyperfine Interact.* **2017**, *238*, 2. [CrossRef]
21. Schell, J.; Lupascu, D.C.; Carbonari, A.W.; Mansano, R.D.; Ribeiro Junior, I.S.; Dang, T.T.; Anusca, I.; Trivedi, H.; Johnston, K.; Vianden, R. Ion implantation in titanium dioxide thin films studied by perturbed angular correlations. *J. Appl. Phys.* **2017**, *121*, 145302. [CrossRef]

22. Wenzel, T.; Bartos, A.; Lieb, K.P.; Uhrmacher, M.; Wiarda, D. Hyperfine interactions of ^{111}Cd in TiO_2 (Rutile) studied by perturbed angular correlations. *Ann. Physik* **1992**, *504*, 155–163. [[CrossRef](#)]
23. Errico, L.A.; Fabricius, G.; Rentería, M.; de la Presa, P.; Forker, M. Anisotropic Relaxations Introduced by Cd Impurities in Rutile TiO_2 : First-Principles Calculations and Experimental Support. *Phys. Rev. Lett.* **2002**, *89*, 055503. [[CrossRef](#)]
24. Ramos, J.M.; Carbonari, A.W.; Costa, M.S.; Saxena, R.N. Electric quadrupole interactions in nano-structured SnO_2 as measured with PAC spectroscopy. *Hyperfine Interact.* **2010**, *197*, 239–243. [[CrossRef](#)]
25. Schell, J.; Lupascu, D.C.; Carbonari, A.W.; Mansano, R.D.; Freitas, R.S.; Gonçalves, J.N.; Dang, T.T.; ISOLDE Collaboration; Vianden, R. Cd and In-doping in thin film SnO_2 . *J. Appl. Phys.* **2017**, *121*, 195303. [[CrossRef](#)]
26. Schell, J.; Lupascu, D.C.; Carbonari, A.W.; Mansano, R.D.; Freitas, R.S.; Gonçalves, J.N.; Dang, T.T.; ISOLDE Collaboration; Vianden, R. Investigation of the local environment of SnO_2 in an applied magnetic field. *Phys. B* **2020**, *586*, 412120. [[CrossRef](#)]
27. Schell, J.; Dang, T.T.; Carbonari, A.W. Incorporation of Cd-Doping in SnO_2 . *Crystals* **2020**, *10*, 35. [[CrossRef](#)]
28. Rentería, M.; Bibiloni, A.G.; Moreno, M.S.; Desimoni, J.; Mercader, R.C.; Bartos, A.; Uhrmacher, M.; Lieb, K.P. Hyperfine interactions of ^{111}In -implanted tin oxide thin films. *J. Phys. Condens. Matter* **1991**, *3*, 3625. [[CrossRef](#)]
29. Wolf, H.; Deubler, S.; Forkel-Wirth, D.; Foettinger, H.; Iwatschenko-Borho, M.; Meyer, F.; Renn, M.; Witthuhn, W.; Helbig, R. Acceptors and Donors in the Wide-Gap Semiconductors ZnO and SnO_2 . *Mater. Sci. Forum* **1986**, *10–12*, 863–868. [[CrossRef](#)]
30. Muñoz, E.L.; Carbonari, A.W.; Errico, L.A.; Bibiloni, A.G.; Petrilli, H.M.; Rentería, M. TDPAC study of Cd-doped SnO. *Hyperfine Interact.* **2007**, *178*, 37. [[CrossRef](#)]
31. Darriba, G.N.; Muñoz, E.L.; Richard, D.; Ayala, A.P.; Carbonari, A.W.; Petrilli, H.M.; Rentería, M. Insights into the aftereffects phenomenon in solids based on DFT and time-differential perturbed $\gamma - \gamma$ angular correlation studies in $^{111}\text{In}(\rightarrow^{111}\text{Cd})$ -doped tin oxides. *Phys. Rev. B* **2022**, *105*, 195201. [[CrossRef](#)]
32. Mercurio, M.E.; Carbonari, A.W.; Cordeiro, M.R.; Saxena, R.N.; D'Agostino, L.Z. Local investigation of hyperfine interactions in pure and Co-doped ZnO. *J. Magn. Magn. Mater.* **2010**, *322*, 1195–1197. [[CrossRef](#)]
33. Mercurio, M.E.; Carbonari, A.W.; Cordeiro, M.R.; Saxena, R.N. Characterization of ZnO and $\text{Zn}_{0.95}\text{Co}_{0.05}\text{O}$ prepared by sol-gel method using PAC spectroscopy. *Hyperfine Interact.* **2007**, *178*, 1–5. [[CrossRef](#)]
34. Dogra, R.; Cordeiro, M.R.; Carbonari, A.W.; Saxena, R.N.; Costa, M.S. Absence of room temperature ferromagnetism in transition metal doped ZnO nanocrystalline powders from PAC spectroscopy. *Hyperfine Interact.* **2010**, *197*, 77. [[CrossRef](#)]
35. Wang, R.; Gardner, J.A.; Evenson, W.E.; Sommers, J.A. Oxygen-vacancy complexes in cerium oxide studied by ^{111}In time-differential perturbed-angular-correlation spectroscopy. *Phys. Rev. B* **1993**, *47*, 638. [[CrossRef](#)]
36. Mowat, J.P.S.; Miller, S.R.; Griffin, J.M.; Seymour, V.R.; Ashbrook, S.E.; Thompson, S.P.; Fairen-Jimenez, D.; Banu, A.-M.; Düren, T.; Wright, P.A. Structural Chemistry, Monoclinic-to-Orthorhombic Phase Transition, and CO_2 Adsorption Behavior of the Small Pore Scandium Terephthalate, $\text{Sc}_2(\text{O}_2\text{CC}_6\text{H}_4\text{CO}_2)_3$, and Its Nitro- And Amino-Functionalized Derivatives. *Inorg. Chem.* **2011**, *50*, 10844–10858. [[CrossRef](#)] [[PubMed](#)]
37. Baldinozzi, G.; Bézar, J.F.; Calvarin-Amiri, G. Rietveld Refinement of Two-Phase Zr-Doped Y_2O_3 . *Mater. Sci. Forum* **1998**, *278–281*, 680–685. [[CrossRef](#)]
38. Marezio, M. Refinement of the Crystal Structure of In_2O_3 at two Wavelengths. *Acta Cryst.* **1966**, *20*, 723–728. [[CrossRef](#)]
39. Haas, H.; Röder, J.; Correia, J.G.; Schell, J.; Fenta, A.S.; Vianden, R.; Larsen, E.M.H.; Aggelund, P.A.; Fromsejer, R.; Hemmingsen, L.B.S.; et al. Free Molecule Studies by Perturbed $\gamma - \gamma$ Angular Correlation: A New Path to Accurate Nuclear Quadrupole Moments. *Phys. Rev. Lett.* **2021**, *126*, 103001. [[CrossRef](#)]
40. Butz, T.; Lerf, A. Comment on “Mössbauer studies of the 6.2 keV γ -rays of ^{181}Ta in Ta-dichalcogenides”. *Phys. Lett. A* **1983**, *97A*, 217–218. [[CrossRef](#)]
41. Ryu, S.; Das, S.K.; Butz, T. Nuclear quadrupole interaction at ^{44}Sc in the anatase and rutile modifications of TiO_2 : Time-differential perturbed angular correlation measurements and *ab initio* calculations. *Phys. Rev. B* **2008**, *77*, 094124. [[CrossRef](#)]
42. Budzinsky, M.; Velichkov, A.I.; Karaivanov, D.V.; Kochetov, O.I.; Salamatin, A.V.; Filosofov, D.V. Use of ^{44}Ti in the Time-Differential $\gamma\gamma$ Perturbed-Angular-Correlation Method for Studying Condensed Matter. *Instrum. Exp. Tech.* **2017**, *60*, 775–781. [[CrossRef](#)]
43. Rentería, M.; Bibiloni, A.G.; Requejo, F.G.; Pasquevich, A.F.; Shitu, J.; Errico, L.A.; Freitag, K. Impurity Cationic-Site Population and Electric-Field Gradient Dependence on Ionic Size in Bixbyites Sesquioxides Implanted With $^{181}\text{Hf} \rightarrow ^{181}\text{Ta}$. *Mod. Phys. Lett. B* **1998**, *12*, 819–827. [[CrossRef](#)]
44. Richard, D.; Rentería, M.; Carbonari, A.W.; Romero, M.; Faccio, R. Preparation of In-doped Y_2O_3 ceramics through a sol-gel process: Effects on the structural and electronic properties. *Ceram. Int.* **2020**, *46*, 16088–16095. [[CrossRef](#)]
45. Sorokin, A.A.; Shirani, E.N.; Shpinkova, L.G.; Akselrod, Z.Z.; Komissarova, B.A.; Ryasny, G.K.; Semyonov, S.I.; Denisenko, G.A.; Zibrov, I.P.; Buev, A.R. PAC studies of the electric quadrupole interaction of ^{181}Ta in yttrium and copper oxides and in superconducting ceramics $\text{YBa}_2\text{Cu}_3\text{O}_{7-\delta}$. *Hyperfine Interact.* **1992**, *73*, 337–346. [[CrossRef](#)]
46. Pasquevich, A.A.; Bibiloni, A.G.; Massolo, C.P.; Rentería, M.; Vercesi, J.A.; Freitag, K. Electric-field gradients at the ^{181}Ta impurity site in Yb, Y, and Dy sesquioxides. *Phys. Rev. B* **1994**, *49*, 14331–14336. [[CrossRef](#)]
47. Uhrmacher, M.; Bolse, W. TDPAC study of indium oxide. *Hyperfine Interact.* **1983**, *15/16*, 445–448. [[CrossRef](#)]
48. Desimoni, J.; Bibiloni, A.G.; Mendoza-Zélis, L.; Pasquevich, A.F.; Sánchez, F.H.; López-García, A. Kinetics studies and oxide characterization in the internal oxidation of AgIn alloys. *Phys. Rev. B* **1983**, *28*, 5739. [[CrossRef](#)]
49. Bibiloni, A.G.; Desimoni, J.; Massolo, C.P.; Mendoza-Zélis, L.; Pasquevich, A.F.; Sánchez, F.H.; López-García, A. Temperature dependence of electron-capture aftereffects in the semiconductor In_2O_3 . *Phys. Rev. B* **1984**, *29*, 1109–1111. [[CrossRef](#)]

50. Bibiloni, A.G.; Massolo, C.P.; Desimoni, J.; Mendoza-Zélis, L.A.; Sánchez, F.H.; Pasquevich, A.F.; Damonte, L.; López-García, A.R. Time-differential perturbed-angular-correlation study of pure and Sn-doped In_2O_3 semiconductors. *Phys. Rev. B* **1985**, *32*, 2393–2400. [[CrossRef](#)]
51. Massolo, C.P.; Desimoni, J.; Bibiloni, A.G.; Mendoza-Zélis, L.A.; Sánchez, F.H.; Pasquevich, A.F.; López-García, A.R. TDPAC studies of after-effects in In_2O_3 precipitates in a silver matrix. *Hyperfine Interact.* **1986**, *30*, 1–8. [[CrossRef](#)]
52. Bolse, W.; Uhrmacher, M.; Lieb, K.P. Perturbed angular-correlation experiments on ^{111}In in oxidized fcc metals and their oxides. *Phys. Rev. B* **1987**, *36*, 1818–1830. [[CrossRef](#)] [[PubMed](#)]
53. Habenicht, S. PAC-studies of Sn-doped In_2O_3 : Electronic defect relaxation following the $^{111}\text{In}(\text{EC})^{111}\text{Cd}$ -decay. *Z. Phys. B* **1996**, *101*, 187–196. [[CrossRef](#)]
54. Ramallo-Lopez, J.M.; Rentería, M.; Miró, E.E.; Requejo, F.G.; Traverse, A. Structure of Extremely Nanosized and Confined In–O Species in Ordered Porous Materials. *Z. Phys. B* **2003**, *91*, 108304. [[CrossRef](#)]
55. Sena, C.; Costa, M.S.; Cabrera-Pasca, G.A.; Saxena, R.N.; Carbonari, A.W. TDPAC measurements in pure and Fe-doped In_2O_3 . *Hyperfine Interact.* **2013**, *221*, 105–110. [[CrossRef](#)]
56. Vercesi, J.A.; Bibiloni, A.G.; Massolo, C.P.; Moreno, M.S.; Pasquevich, A.F.; Freitag, K. Hyperfine characterization of ^{181}Ta in In_2O_3 . *Phys. Rev. B* **1993**, *41*, 490–492. [[CrossRef](#)] [[PubMed](#)]
57. Renteria, M.; Requejo, F.G.; Bibiloni, A.G.; Pasquevich, A.F.; Shitu, J.; Freitag, K. Perturbed-angular-correlation study of the electric-field gradient in ^{181}Hf -doped and implanted indium sesquioxide. *Phys. Rev. B* **1997**, *55*, 14200–14207. [[CrossRef](#)]
58. Atkins, P.W.; Overton, T.L.; Rourke, J.P.; Weller, M.T.; Armstrong, F.A. *Shriver and Atkins' Inorganic Chemistry*, 5th ed.; Oxford University Press: Oxford, UK, 2010; pp. 783–784.
59. Aleshina, L.A.; Loginova, S.V. Rietveld analysis of X-ray diffraction pattern from $\beta\text{-Ta}_2\text{O}_5$ oxide. *Crystallogr. Rep.* **2002**, *47*, 415–419. [[CrossRef](#)]
60. Stephenson, N.C.; Roth, R.S. The Crystal Structure of the High Temperature Form of Ta_2O_5 . *J. Solid State Chem.* **1971**, *3*, 145–153. [[CrossRef](#)]
61. Autschbach, J.; Zheng, S.; Schurko, R.W. Analysis of Electric Field Gradient Tensors at Quadrupolar Nuclei in Common Structural Motifs. *Inc. Concepts Magn. Reson. Part A* **2010**, *36A*, 84–126. [[CrossRef](#)]
62. Blaha, P.; Schwarz, K.; Dederichs, P.H. First-principles calculation of the electric-field gradient in hcp metals. *Phys. Rev. B* **1988**, *37*, 2792–2797. [[CrossRef](#)] [[PubMed](#)]